https://dx.doi.org/10.1016/j.tws.2024.111594

Numerical simulation of corroded circular hollow section steel columns: A corrosion evolution approach

Yun Zhao [a], Xuhong Zhou [a], Fei Xu [a*], Tak-Ming Chan [b]

[a] School of Civil Engineering, Chongqing University, Chongqing, China

[b] Department of Civil and Environmental Engineering, The Hong Kong Polytechnic University, Hong Kong, China

Abstract

This study introduces a numerical simulation method for corroded circular hollow section steel columns, utilising a newly developed corrosion evolution model. This model was formulated by characterising the corrosion morphology and calibrating parameters throughout the entire corrosion process. An interpolation method was implemented to estimate the number of corrosion pits, based on experimentally measured corrosion ratios. Consequently, this allowed for the numerical prediction of the time-varying corrosion morphologies. Finite element (FE) models, incorporating this corrosion evolution model, were constructed. These corroded column models underwent validation through comparison with experimental findings. To further establish the effectiveness of the proposed FE models in predicting the structural behaviour of corroded members, FE models were also developed using the traditional uniform thickness reduction approach for comparative analysis. The results revealed that the proposed FE models for corroded structures offer a more accurate prediction of mechanical performance, particularly in instances of severe corrosion damage.

Keywords: corroded member, corrosion morphology, corrosion pit, evolution, finite element model, pit number

* Corresponding author.
E-mail address: fei.xu@cqu.edu.cn (F. Xu).

1 Introduction

Circular hollow section (CHS) steel columns are crucial load-bearing elements in various structures, including bridges, oil platforms, and wind turbines. Despite protective anticorrosive coatings, these columns are prone to corrosion in marine, industrial, and atmospheric environments [1–2]. Corrosion often leads to a reduction in cross-sectional area and heightened stress concentration due to unevenly distributed pits [3–5]. This is particularly problematic for thin-walled structures like CHS steel columns, where both uniform thickness reduction and pit defects significantly impact their integrity. Consequently, assessing the residual mechanical behaviour of corroded CHS steel columns is of paramount importance.

Numerous experimental studies have examined the mechanical behaviour of CHS steel columns exposed to chloride solutions in accelerated corrosion tests over periods ranging from 1 to 15 months [6–8]. These studies noted substantial variability in yield and ultimate strengths of corroded members, attributable to randomly occurring corrosion morphologies and limited data availability. Furthermore, the location of severe corrosion impacts the failure mode of the structural members [7–10], with global and local buckling occurring prematurely in specimens exhibiting severe mid-length corrosion and circumferential band corrosion, respectively.

Generally, the random distribution of corrosion morphologies can be ascribed to the stochastic nature of corrosion pit initiation and growth mechanisms. Past experiments suggest that pit initiation and development follows probabilistic models, such as the nonhomogeneous Poisson process [11] and the nonhomogeneous Markov process [11–12]. Consequently, several pit evolution models have been proposed [13–14] to simulate the progression of corrosion morphology in metals. Nevertheless, most models focus on single-pit evolution, overlooking scenarios like multi-pit overlap leading to uniform thickness reduction in severe corrosion cases.

Accelerated corrosion tests, while faster than in-field corrosion, are resource-intensive, requiring repeated testing and extensive data collection throughout a structure's lifetime. Many numerical simulations simplify this process by adopting the uniform thickness reduction method in finite element (FE) models [8, 15–16], but this often underestimates stress concentration caused by corrosion pits [17]. Recent research efforts have shifted towards incorporating pit geometry and evolution in FE models to achieve more accurate predictions of structural performance in corroded

members [13–14, 18–20]. These studies primarily used artificially generated pits and pit groups, not fully accounting for key aspects of corrosion morphology, such as randomness and multi-pit interactions. This gap has led to discrepancies in the mechanical performance of corroded members between numerical and experimental results, as noted in previous studies. However, the random distribution of pit evolution in corrosion morphology has yet to be considered comprehensively.

In this study, we proposed a numerical simulation approach designed to accurately and efficiently evaluate the mechanical behaviour of corroded column members. This method accounted for the random distribution of pit evolution in corrosion morphology. The corrosion evolution model was formulated by characterising the corrosion morphology and calibrating parameters throughout the entire corrosion process. Utilising this model, time-varying corrosion morphologies were integrated into the FE models. These models of the corroded column specimens were then validated through comparison with experimental results. Additionally, to underscore the enhanced effectiveness of our numerical simulation method compared to traditional techniques, a comparative analysis between our proposed method and the conventional uniform thickness reduction FE models was conducted.

2 Corrosion evolution model and parameters

2.1 Corrosion evolution models

2.1.1 Evolution model of a single pit

The evolution law of a single pit was investigated in previous experimental studies using in-situ observation methods [21–23]. Figs. 1(a) and (b) display the corrosion morphology of a single pit on a 304 stainless steel plate at 1500 s and 6000 s, respectively [22]. These images illustrate that the pit expands in both width and depth over time. Consequently, a single pit evolution model was developed [24], drawing on these experimental observations and summarised in Fig. 2. The model proposed a semi-ellipsoidal pit shape [24–25], with the pit depth (T_p) and width (b) increasing with time, alongside the increments ΔT_p and Δb.

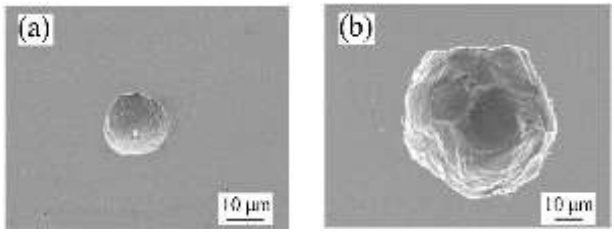

(a) 1500s (b) 6000s

Fig. 1. Pit morphology of as-received stainless steel 304 after pitting initiation [22].

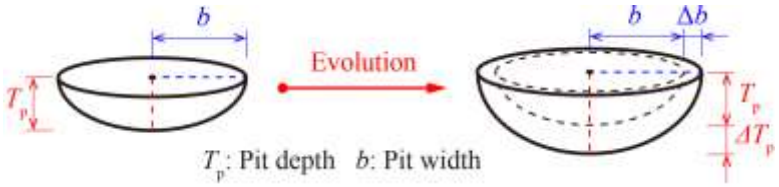

Fig. 2. Single pit evolution model [24].

2.1.2 Evolution model of multi-pits

Electrochemical experiments have shown that once pitting corrosion begins on a metal surface, the number of pits remains constant [26–27], while the corrosion rate increases due to single pit expansion [28], as detailed in Section 2.1.1. This behaviour has been observed in various metals, such as ferritic stainless steel [27] and AA2024-T3 aluminium [29], as depicted in Figs. 3(a) and (b). Thus, it is assumed that the number of pits in the corrosion morphology remains unchanged throughout their evolution.

(a) Ferritic stainless steel surface close to the anodic electron [27].

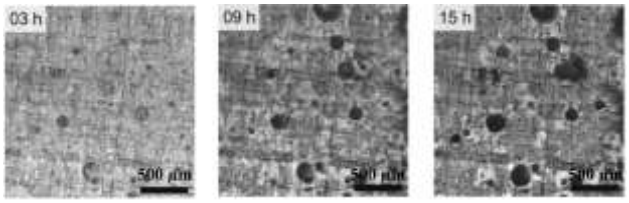

(b) AA2024-T3 aluminium surface after immersion in NaCl solution [29].

Fig. 3. Evolution process of multi-pits at different times.

As individual pits develop, they tend to overlap, resulting in a uniform reduction of thickness [21]. Fig. 4 illustrates a schematic diagram of the corrosion morphology in a cross-sectional view. For Pit A, T_{cA} and T_{uA} represent the maximum vertical distances from the original non-corroded surface to the inner coarse surface of Pit A and the uniform corrosion depth, respectively. Thus, the pit depth of Pit A (T_{pA}) is defined as the difference between T_{uA} and T_{cA}. This definition of pit depth is commonly used in numerical models to account for the effects of adjacent pit overlap, leading to a potentially unsafe assessment of mechanical behaviour [30]. This is due to the fact that the uniform corrosion depth, T_u, is not considered. To address this, considering the uniform corrosion depth T_u and keeping the pit aspect ratio R_a (i.e., the ratio of $2b$ to T_p in Fig. 2) constant, T_p is increased to T_c as the pit depth in the multi-pit evolution model.

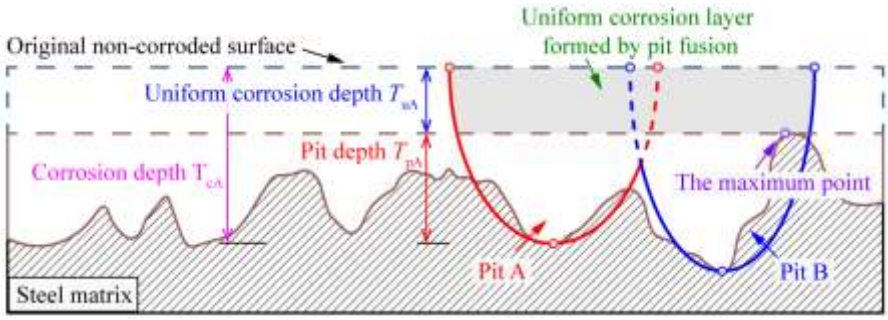

Fig. 4. Schematic diagram of the 2D morphology of the corroded steel matrix surface.

The pit depth T_c and aspect ratio R_a are modelled to follow a lognormal distribution [26, 31] and are represented by the expectations of these distributions. The standard deviation S_T of the pit depth remains constant [25], while the pit position follows a uniform distribution. The aspect ratio R_a stays constant at a given time but varies over time. The relationship between thickness loss T_L (the product of mass loss rate and initial thickness T_0 of the specimen), T_c, R_a, and time t follows a power function [24–25], as defined in Eqs. (1)–(3). Note that Eqs. (1) to (3) are applicable to structures without protective coatings.

$$T_L = A_1 \times t^{n_1} \tag{1}$$

$$T_c = A_2 \times t^{n_2} \tag{2}$$

$$R_a = A_3 \times t^{n_3} \tag{3}$$

where A_1, A_2, A_3, n_1, n_2, and n_3 represent the parameters that influence the curve shape.

2.2 Corrosion parameters during the evolution

The proposed pit corrosion evolution model was validated using experimental results from Q235 steel subjected to wet/dry cyclic accelerated corrosion tests [26]. Parameters such as thickness loss T_L, uniform corrosion thickness T_u, pit depth T_p, and pit aspect ratio R_a were extracted and counted using the CroEva program [26] from corrosion morphologies obtained by a PS50 non-contact 3D profiler with 0.05 mm accuracy at different corrosion times, as listed in Table 1. The average value of the fluctuating standard deviation S_T was determined to be 0.272, reflecting the variation in pit depths. The parameters A_1, A_2, A_3, n_1, n_2, and n_3 in Eqs. (1)–(3) were calibrated using the test data [26], as tabulated in Table 2. Consequently, the parameters T_L, T_c, and R_a could be calculated using the calibrated equations (Eqs. (1)–(3)). Table 1 compares these parameters' values from the tests and calculations, showing a Pearson correlation coefficient (ρ) greater than 0.92. This indicates that the corrosion evolution model can accurately and reliably predict the corrosion parameters T_L, T_c, and R_a as obtained from the tests.

The corrosion parameters are governed by a specific distribution rule, and some parameters evolve in relation to others. Hence, it is plausible to assume that the pit depth and aspect ratio at a given time i ($T_{c,i}$ and $R_{a,i}$, respectively) evolve linearly with the corresponding thickness loss ($T_{L,i}$), as expressed in Eq. (4a). Following Eqs. (1) to (3), the parameters $A_{1,i}$, $A_{2,i}$, $A_{3,i}$, $n_{1,i}$, $n_{2,i}$, and $n_{3,i}$ adhere to relationships outlined in Eqs. (4b) and (4c). Consequently, the corrosion parameters $T_{c,i}$ and $R_{a,i}$ can be deduced based on the test measurements of T_L, T_c, and R_a at a specific time, as detailed in Table 2. The thickness loss $T_{L,i}$ should be determined from tests beforehand. Fig. 5 depicts the predicted T_c and R_a using Eqs. (4a)–(4c), illustrating a consistency with the test results, thereby validating Eq. (4) for calculating the necessary parameters for corrosion evolution. Notably, when the thickness loss T_L is measured in the test, the pit depth and aspect ratio can be calculated using the proposed Eqs. (4a)–(4c), in conjunction with a set of fundamental corrosion parameters calibrated as listed in Table 2. The pit depth, following a lognormal distribution, can then be generated using the calculated expectation of $T_{c,i}$ and the standard deviation of 0.272.

Table 1 Corrosion parameters obtained from the tests [26]

T	T_L (mm)		T_u	T_p (μm)		S_T		R_a			T_c (μm)		
(day)	Test	Eq. (1)	(μm)	Side A	Side B	Side A	Side B	Side A	Side B	Eq. (2)	Side A	Side B	Eq. (3)
30	0.0572	0.0800	0	96.544	81.451	0.26	0.19	10.59	10.07	9.42	96.544	81.451	108.294
70	0.1871	0.1530	40	202.350	239.847	0.21	0.32	4.48	4.18	5.60	242.257	279.779	195.472
110	0.2759	0.2161	95	281.463	139.770	0.25	0.38	3.49	4.62	4.24	376.531	234.862	267.857
150	0.2909	0.2740	65	270.426	270.426	0.21	0.48	3.32	4.76	3.51	335.291	335.291	332.497
250	0.3464	0.4050	125	323.759	281.463	0.39	0.20	2.77	3.07	2.56	448.541	406.263	474.696
310	0.3857	0.4775	160	320.538	265.072	0.29	0.38	2.66	3.19	2.24	480.583	424.962	551.481
370	0.5455	0.5467	210	343.779	487.846	0.23	0.21	2.14	1.79	2.01	553.909	697.847	623.862
440	0.6935	0.6242	200	459.436	765.095	0.20	0.15	1.60	1.19	1.81	659.182	964.876	703.944
ρ	0.96	-	-	-	-	-	-	0.97	0.95	-	0.97	0.92	-

Note: Side A and side B are two surfaces of a steel plate, and ρ is the Pearson correlation coefficient.

Table 2 Fitting results of T_L, T_c, and R_a parameters

T_L (mm)			T_c (μm)			R_a		
A_1	n_1	R^2	A_2	n_2	R^2	A_3	n_3	R^2
0.00593	0.765	0.907	10.117	0.697	0.893	76.008	-0.614	0.857

The entire corrosion evolution process in corroded steel members, encompassing initial slight and moderate pitting to severe corrosion with a uniform corrosion layer and pits, can be accurately replicated using the proposed corrosion evolution model, parameters, and associated assumptions.

$$\frac{T_{\mathrm{L},i}}{T_{\mathrm{L}}}=\frac{T_{\mathrm{c},i}}{T_{\mathrm{c}}}=\frac{R_{\mathrm{a},i}}{R_{\mathrm{a}}} \tag{4a}$$

$$\frac{A_{1,i}}{A_1}=\frac{A_{2,i}}{A_2}=\frac{A_{3,i}}{(A_3)^a} \tag{4b}$$

$$n_{1,i}-n_1=n_{2,i}-n_2=n_{3,i}-an_3 \tag{4c}$$

where $T_{\mathrm{L},i}$, $T_{\mathrm{c},i}$, and $R_{\mathrm{a},i}$ represent a set of parameters related to thickness loss, pit depth, and aspect ratio, along with their corresponding parameters of $A_{1,i}$, $A_{2,i}$, $A_{3,i}$, $n_{1,i}$, $n_{2,i}$, and $n_{3,i}$. It is important to note that these parameters differ from those listed in Table 2, i.e., $T_{\mathrm{L},i}=A_{1,i}t^{n_{1,i}}$, $T_{\mathrm{c},i}=A_{2,i}t^{n_{2,i}}$, $R_{\mathrm{a},i}=A_{3,i}t^{n_{3,i}}$. The factor a initially equals 1 but changes to -1 when the absolute value of $n_{3,i}$ falls below 0.6.

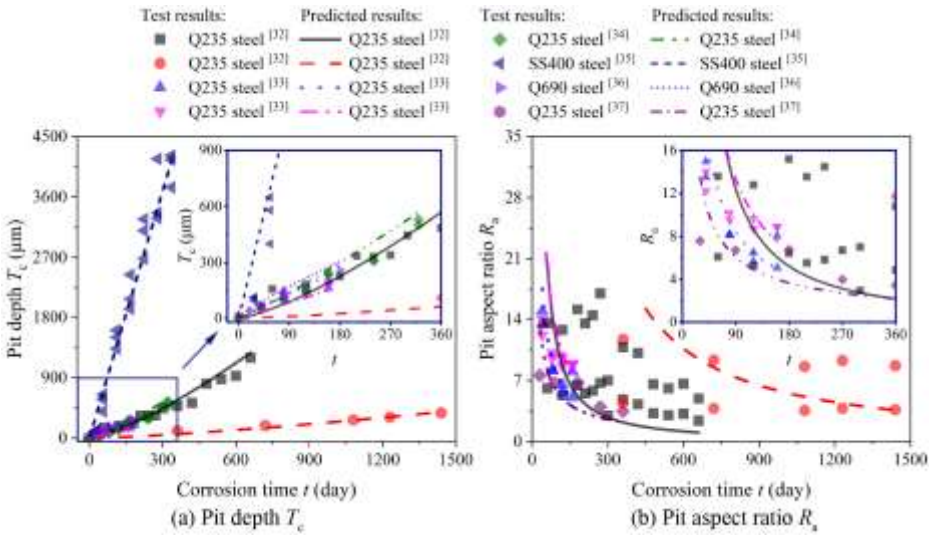

Fig. 5. Predictions of parameters of T_{c} and R_{a} [32 – 37].

3 Numerical simulation of corrosion morphology evolution

Determining the corrosion morphologies initially requires knowing the number of corrosion pits. In the previously proposed corrosion evolution model [24], the number of pits was deduced from the initial period's thickness loss, and the pit aspect ratio was held constant, differing from test

findings [26]. Therefore, this study employed an interpolation method that iteratively fine-tuned the pit count to closely match the experimental results. This approach allowed for a more precise prediction of the experimental results by continuously refining the estimation of the number of pits.

3.1 Calculation of the number of corrosion pits

3.1.1 General procedure of the proposed pit number calculation programme

The comprehensive steps for calculating the number of corrosion pits are outlined below, with a schematic representation provided in Fig. 6:

(a) The NumPy package within the Python programming environment is utilised for essential functions.

(b) The RandomState function is employed to log the random pit depths and positions in the initial stage of evolution. The lognormal function is applied to manage the parameter T_L, followed by the use of the uniform function to regulate the pit position.

(c) Key corrosion parameters are inputted, including the random state starting point m, the expected pit depth μ (equivalent to T_c), the standard deviation σ (equal to S_T), and the area over which pits are distributed.

(d) An initial range of pit numbers (n_{down}, n_{up}) that align with the measured thickness loss in the test is estimated. These values, n_{down} and n_{up}, are then utilised as the lower and upper bounds, respectively, for further iterations to determine the accurate pit number.

(e) During each iteration, the thickness loss T_{Lk} is evaluated to ascertain if it meets the required thickness loss T_{Li}. If it does not, the pit number n_k and the corresponding thickness loss T_{Lk} are recorded.

(f) A quantitative relationship between the thickness loss T_{Lk} and the pit number n_k is established, as illustrated in Eq. (5) [24, 30]. This is achieved when T_{Lk} equals T_{Li}. Using the developed programme depicted in Fig. 6, the number of corrosion pits at each specific time can be accurately and reliably determined, culminating in the calculation of the ultimate pit number throughout the corrosion evolution process.

$$n = B\ln\left(1 + CT_L\right) \tag{5}$$

where B and C are the coefficients controlling the function curve shape.

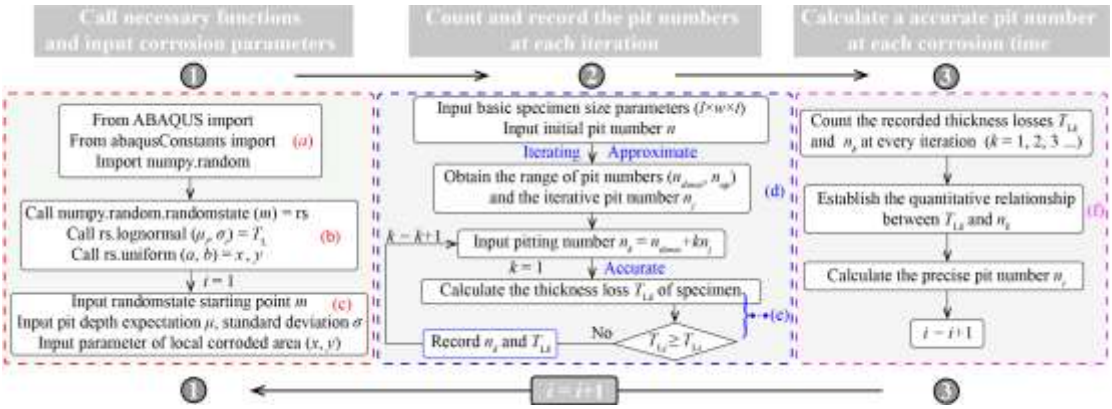

Fig. 6. Schematic view of numerically reproducing a corrosion morphology.

3.1.2 Verification of the proposed pit number calculation programme

The corrosion parameters T_L, T_C, and R_a, as listed in Table 2, were utilised to systematically examine the process of establishing a correlation between pit number and thickness loss. It is important to note that the thickness losses for all specimens should not exceed half of their initial thickness [38], likely due to the protective effect of rust layers. The maximum corrosion duration was 1800 days, with a one-sided thickness loss of 1.833 mm, calculated using Eq. (1) with parameters from Table 2. This loss represents 50.57% of the original 7.25 mm thickness [39]. Both the length and width of the pit distribution area are set at 50 mm. To minimise variation in the calculated thickness loss values, the programme was run five times, with the average value being adopted [24].

The lower and upper limits for the number of pits, i.e., n_{down} and n_{up}, were set at 400 and 4000, respectively, for the interpolation and iteration processes. The thickness loss was then calculated at each increment of 400 pits, with the results displayed in Fig. 7(a). It was observed that the variation in the results from five repeated calculations was negligible, and the calculated thickness loss approached the test results as the pit number increased, demonstrating the effectiveness of this method. The experimentally measured thickness losses fell between the calculated thickness losses for pit numbers of 3200 and 4000. Consequently, the pit number range was narrowed to 3200 to 4000, and an iteration process with increments of 40 pits per iteration was implemented. The average recorded thickness loss and corresponding pit number at specific corrosion times were then regressed using Eq. (5). The associated parameters B and C in Eq. (5) are listed in Table 3, where

the correlation coefficients (R^2) all exceed 0.996, indicating a high degree of fitting accuracy. Fig. 7(b) and Table 3 show the number of pits that correspond to the measured thickness loss at various corrosion times. Notably, the pit count decreases with increasing corrosion time, particularly in the initial period, likely due to the expansion and merging of adjacent shallow and narrow pits [26]. In this study, a minimum pit number of 3463, with an absolute error under 5%, was selected to balance calculation accuracy and computational effort.

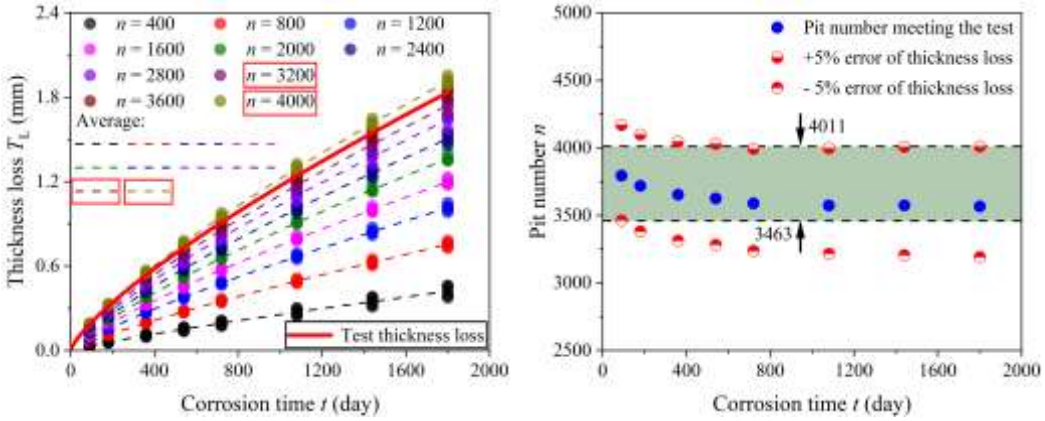

(a) Counted thickness losses at different pit numbers (b) Fluctuation range of the pit number

Fig. 7. Pit number at different corrosion times.

Table 3 Results of parameter fitting and pit number at different corrosion times

Corrosion time t (day)	B	C	R^2	Thickness loss T_L (mm)	Pit number n	Corrosion time t (day)	B	C	R^2	Thickness loss T_L (mm)	Pit number n
90	-3496.50	-3.57	0.998	0.1854	3795	720	-2695.42	-0.81	0.997	0.9097	3590
180	-3194.89	-2.18	0.998	0.3150	3719	1080	-2570.69	-0.61	0.997	1.2406	3574
360	-2881.84	-1.34	0.997	0.5353	3654	1440	-2487.56	-0.49	0.997	1.546	3575
540	-2808.99	-0.99	0.997	0.7300	3626	1800	-2421.31	-0.42	0.996	1.8337	3567

3.2 Establishment of corrosion evolution morphologies

This section focuses on developing the corrosion evolution morphologies for steel tensile

coupons and steel CHS short and long columns.

3.2.1 Specimen dimensions

The dimensions of the steel tensile coupons [39] are illustrated in Fig. 8(a). The initial thickness of these non-corroded specimens was the measured minimum cross-sectional thickness from the tests, i.e., 7.25 mm. The gauge length segment measured 50 mm in length and 25 mm in width. The dimensions of the steel short and long columns were derived from previous studies [6,8], as shown in Figs. 8(b) and (c). It is important to note that the corroded areas on the long columns were numerically labelled to differentiate between specimens, as depicted in Fig. 9.

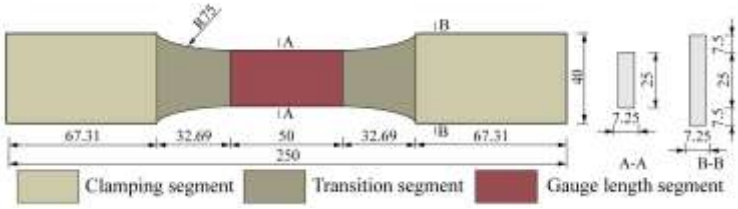

(a) Tensile coupon specimen

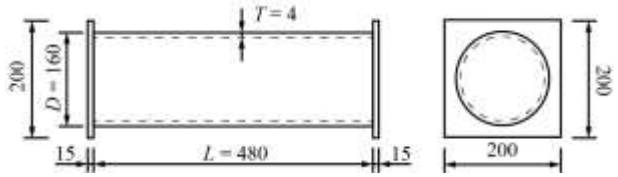

(b) Steel tube short column specimen

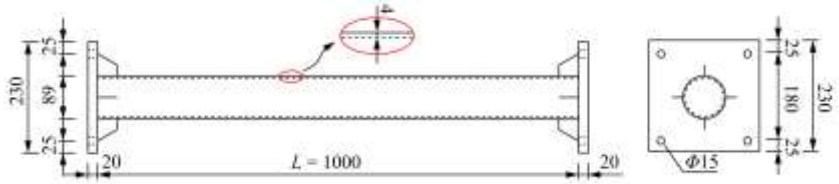

(c) Steel tube long column specimen

Fig. 8. Details of specimens (unit: mm).

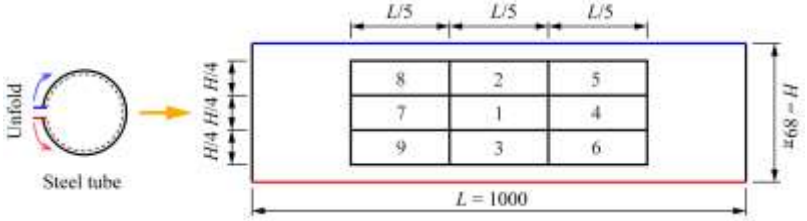

Fig. 9. Numbering of corroded areas of the tube specimen (unit: mm).

265 3.2.2 Calculation of the pit numbers

266 The corrosion parameters for circular steel short and long columns are listed in Table 4.
267 Thickness loss T_L values at different corrosion times, obtained from tests [6, 8], were used to
268 calculate the pit depth and aspect ratio over time using Eqs. (1) – (4), with the parameters detailed
269 in Table 5. Following the method outlined in Section 3.2, the pit numbers for the short column and
270 per corroded area on the long column were calculated to be 103076 (for the entire model) and 3289,
271 respectively.

272

273 Table 4 Summary of corrosion parameters of steel columns

	Specimen	Time t (days)	Thickness loss T_L (mm)	Thickness loss rate (%)	Specimen	Time t (days)	Thickness loss T_L (mm)	Thickness loss rate (%)
Short	CST-M1	30	0.0924	2.31	CST-M3R	90	0.2680	6.70
columns	CST-M2	60	0.1752	4.38	CST-M4	120	0.3016	7.54
[6]	CST-M3	90	0.2656	6.64	CST-M4R	120	0.3028	7.57
	H1L1-90	90	0.2734	6.84	H3L1-180	180	0.5467	13.67
Long	H2L3-90	90	0.2781	6.95	H1L2-270	270	0.6773	16.93
columns	H3L2-90	90	0.2936	7.34	H2L1-270	270	0.5835	14.59
[8]	H1L3-180	180	0.5383	13.46	H3L3-270	270	0.7491	18.73
	H2L2-180	180	0.5324	13.31				

274

275 Table 5 Results of corrosion parameter fitting of corroded specimens

Sample	T_L (μm)			T_c (μm)			R_a		
	A_1	n_1	R^2	A_2	n_2	R^2	A_3	n_3	R^2
Tensile coupon	0.00593	0.765	0.907	10.117	0.697	0.893	76.008	-0.614	0.857
Short column	0.00819	0.760	0.970	13.973	0.692	-	104.976	-0.619	-
Long column	0.00899	0.776	0.907	15.186	0.708	-	114.008	-0.603	-

276

277 3.2.3 Establishment of the corrosion morphologies

Figs. 10(a) and (b) depict the progression of corrosion morphology on the tensile coupon over corrosion periods ranging from 70 to 440 days. It is evident that individual pits tend to merge with adjacent ones as corrosion progresses, closely mirroring observations from the test results [26]. Figs. 11 and 12 show the developed corrosion morphologies on the corroded short and long columns at specific times. Notably, the expansion of corrosion is less pronounced. This can be attributed to two factors: (1) as corrosion time lengthens, the growth rate of thickness loss diminishes due to the protective qualities of the dense rust layer, and (2) the rate of increase in pit depth surpasses that of the pit width [26].

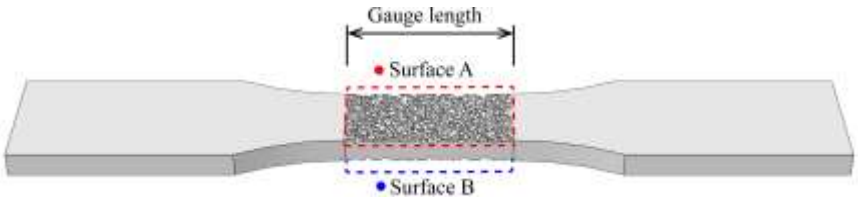

(a) Corroded area

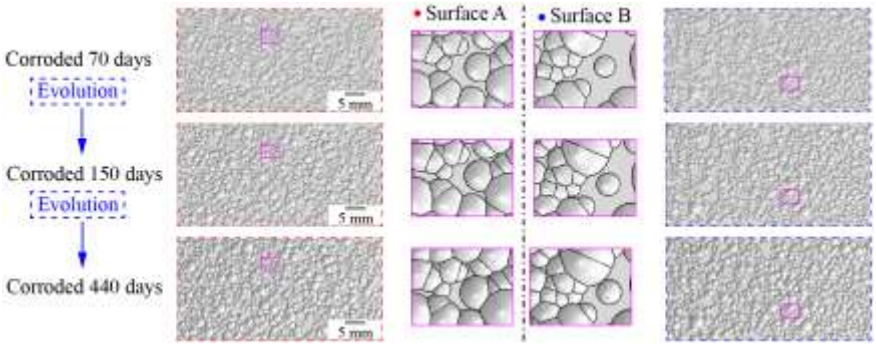

(b) Morphologies on the corroded surface

Fig. 10. Corrosion evolution model of the tensile coupon specimen.

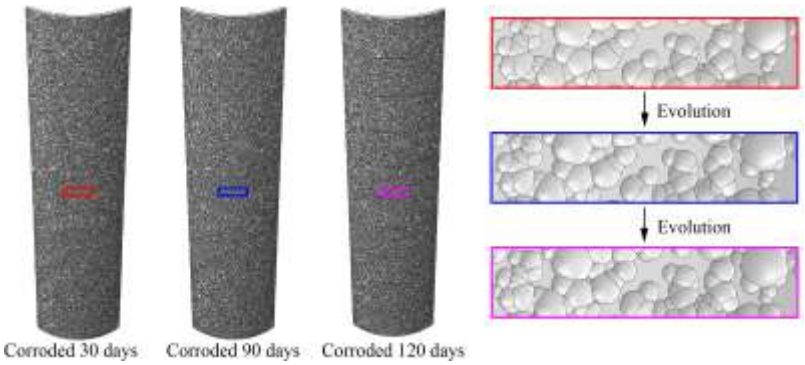

Fig. 11. Corrosion evolution model of the steel CHS short column.

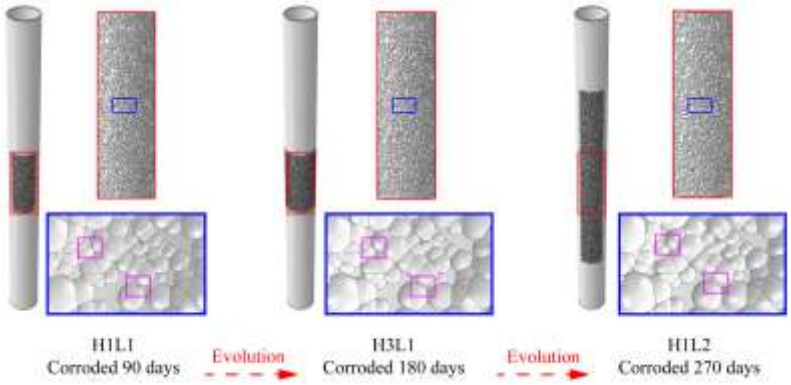

Fig. 12. Corrosion evolution morphologies of the steel CHS long column.

3.3 Summary of the proposed method to predict corrosion evolution

Fig. 13 presents a comprehensive flow chart of the developed corrosion evolution model. Drawing on microscopic observations of actual pit development and incorporating reasonable assumptions, the models for both single pit and multi-pit evolution were formulated, with the relevant equations outlined in Eqs. (1) – (4). An interpolation approach, integrated with a Python programme, was employed to calculate the number of pits characterising the corrosion morphologies throughout the evolution process. The resultant corrosion morphologies of the steel members can then be incorporated into FE models to further investigate their mechanical behaviour.

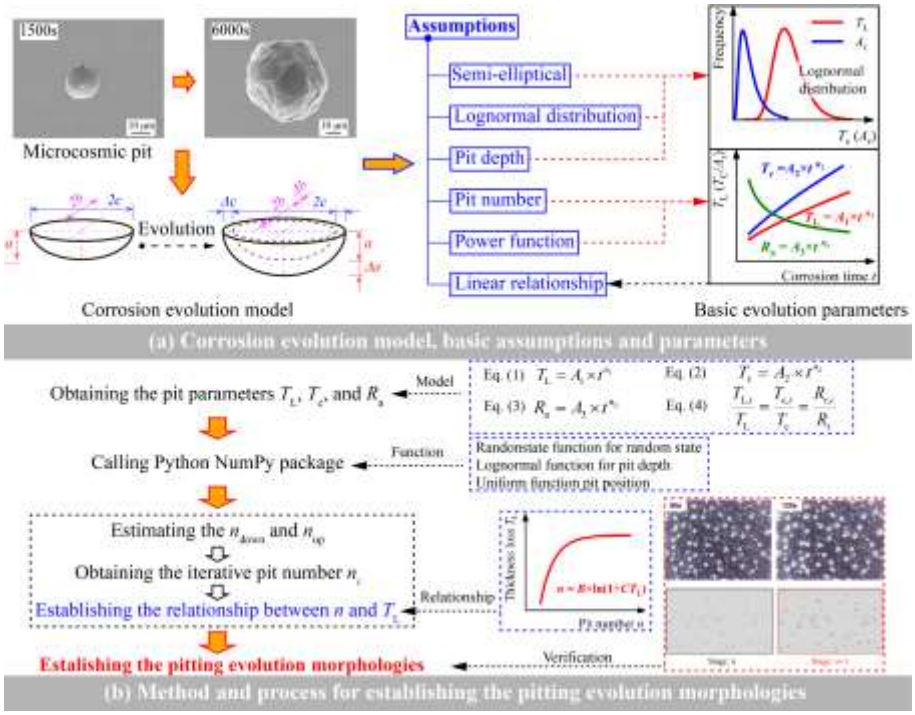

Fig. 13. General flow chart of corrosion evolution.

4 Finite element models

The models of corroded specimens were developed using the proposed corrosion evolution method. This section comprehensively details the constitutive models, boundary and loading conditions, initial imperfections, and mesh sensitivity analysis.

4.1 Constitutive models

The stress-strain curve of Q235 steel, derived from non-corroded specimens [39], is depicted in Fig. 14(a). The engineering stress-strain curves were transformed into true stress-strain curves using Eqs. (6) – (7), as shown in Fig. 14(a). Post-necking true stress was determined using modifications expressed in Eq. (8), assuming a linear hardening modulus [40] and building on prior research [41]. The stress-strain curve for Q460 steel [6] from the non-corroded steel CHS short column is displayed in Fig. 15.

The factor w was obtained using iteration and trial methods, validated against experimental results. A modified multi-segment linear model served as the constitutive model. The factor w at various true strains is presented in Fig. 14. Fig. 14(b) illustrates the stress-strain curves derived from experimental and numerical findings, showing strong concordance. Notably, the maximum true strain is calibrated to 1.31 using Eq. (8) and is considered the fracture strain for determining the fracture state of the tensile coupon specimen [42]. Sensitivity analyses revealed that the impact of factor w on the mechanical behaviour of a steel CHS short column is minimal; therefore, w was set as 1.0 in this constitutive model.

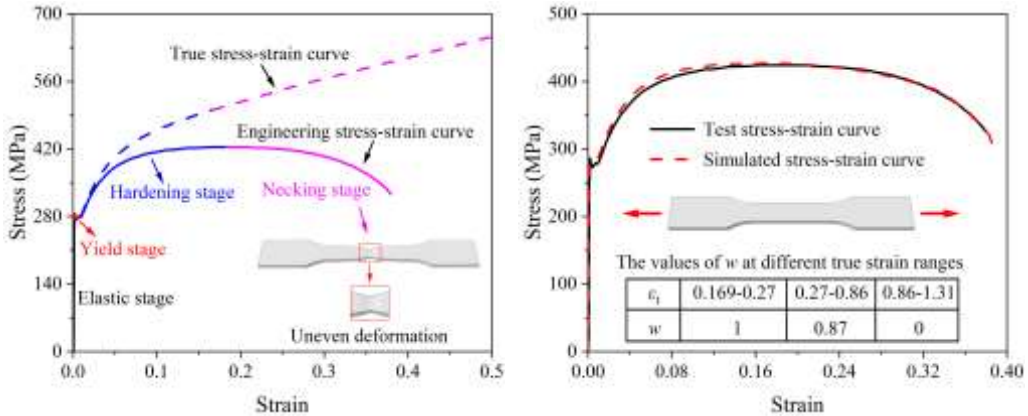

(a) Stress-strain curve (b) Verification of the stress-strain curve

Fig. 14. Constitutive model of Q235 steel.

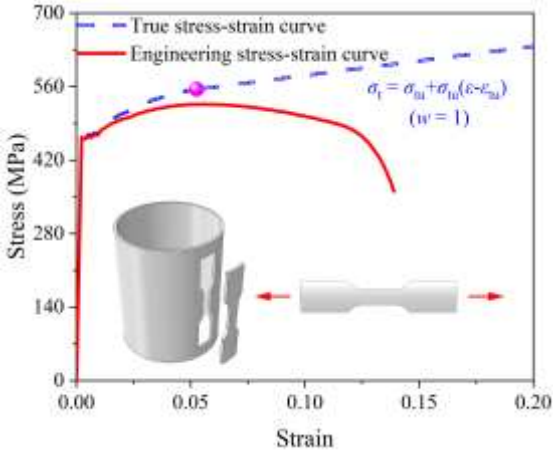

Fig. 15 Stress-strain curve of Q460 steel

$$\sigma_t = \sigma_e(1+\varepsilon_e) \tag{6}$$

$$\varepsilon_t = \ln(1+\varepsilon_e) \tag{7}$$

$$\sigma_t = \sigma_{tu} + w\sigma_{tu}(\varepsilon - \varepsilon_{tu}) \tag{8}$$

where σ_t and ε_t are the true stress and strain, σ_e and ε_e are the engineering stress and strain, and σ_{tu} and ε_{tu} are the true stress and strain at the necking point.

For CHS long columns, the stress-strain relationship was not reported [8], so the engineering stress-strain relationship proposed by Yun and Gardner [43], expressed in Eq. (9), was adopted. Measured values for yield strength (f_y), ultimate strength (f_u), and elastic modulus (E)—343 MPa, 481 MPa, and 201 GPa, respectively [44]—were used. True stress and strain were calculated using Eqs. (6) – (7), excluding the post-necking true stress-strain curve.

$$f(\varepsilon_e) = \begin{cases} E\varepsilon & \varepsilon \le \varepsilon_y \\ f_y & \varepsilon_y < \varepsilon \le \varepsilon_{sh} \\ f_y + \left(f_u - f_y\right)\left[0.4\alpha + 2\alpha / \left(1+400\alpha^5\right)^{0.2}\right] & \varepsilon_{sh} < \varepsilon \le \varepsilon_u \end{cases} \tag{9}$$

where f_y is the yield strength, f_u is the ultimate strength, E is the elastic modulus, $\alpha = (\varepsilon-\varepsilon_{sh})/(\varepsilon_u-\varepsilon_{sh})$, $\varepsilon_{sh} = 0.1f_y/f_u-0.055$ and $0.015 \le \varepsilon_{sh} \le 0.03$, and $\varepsilon_u = 0.6(1-f_y/f_u)$ and $\varepsilon_u \ge 0.06$.

4.2 Boundary and loading conditions

Full FE models were developed for the tensile coupons and long columns, as illustrated in Figs. 16(a) and (b). For the short columns, to enhance computational efficiency, quarter models using

symmetric lines were created, as shown in Fig. 16(c). Each column end was affixed to rigid endplate, with the end constraint and compressive load applied on the reference points of each endplate, following the test setup [6, 8], as depicted in Figs. 16(b) and (c). In the long column models, the hinge centre's distance from the endplate, denoted as *K*, was examined to determine the actual calculation length for each specimen. The results of this sensitivity study are shown in Fig. 17, with *K* established at 30 mm for this study.

(a) Tensile coupon specimen

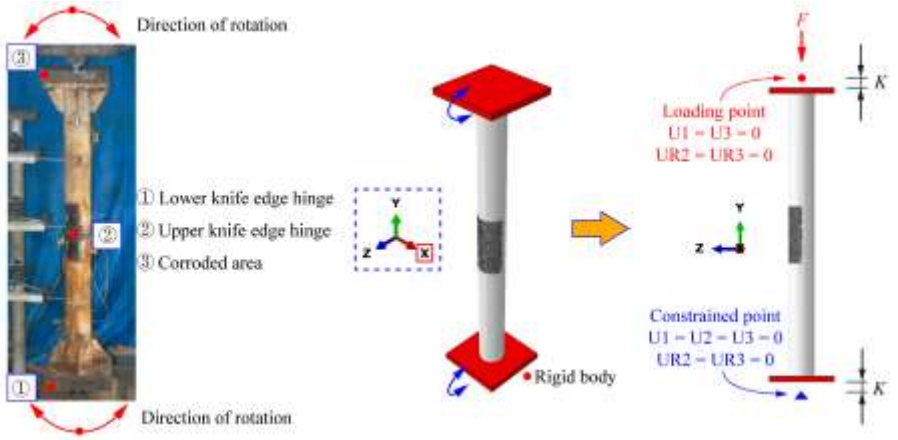

(b) Steel tube long column

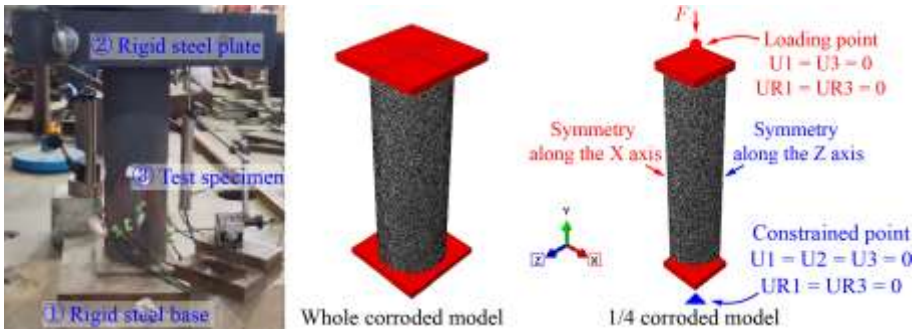

(c) Steel tube short column

Fig. 16. Loading and boundary conditions.

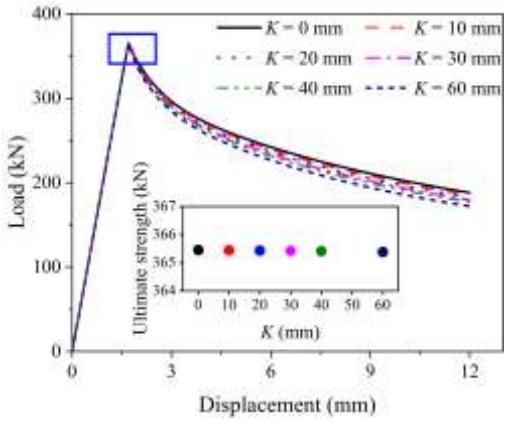

Fig. 17. Sensitivity analysis of the K value.

4.3 Initial imperfections

The impact of cold-forming residual stresses, as well as global and local geometrical imperfections, on the load-displacement curves of CHS columns was evaluated. The global geometrical imperfections of the steel CHS long column were aligned with the test specifications [8], and residual stress was deemed negligible due to its release post corrosion [45]. A sensitivity analysis on local geometrical imperfections was conducted, employing values of I_L ranging from $T_0/50$ to $T_0/500$ [46], where T_0 represents the initial nominal thickness. The simulation results, depicted in Fig. 18, indicate that local geometrical imperfections could be disregarded in this study. This is because local geometrical imperfections were considerably smaller than the local corrosion defects, with local pit depths reaching 0.8 mm at a corrosion time of 90 days [6], approximately $1/5T_0$. This significantly impacts the ultimate strength of the steel columns. Moreover, the load-displacement curves of steel CHS long columns are predominantly influenced by initial global geometrical imperfections rather than local geometrical imperfections.

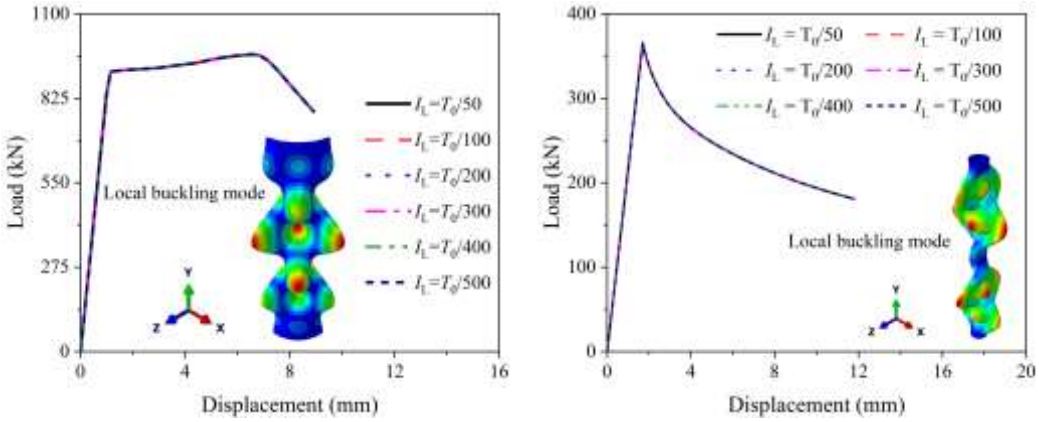

(a) Steel CHS short column (b) Steel CHS long column

Fig. 18. Load-displacement curves with different local geometric initial imperfections.

4.4 Mesh sensitivity

For the FE models, 10-node quadratic tetrahedral elements (C3D10) were utilised. A mesh sensitivity analysis was carried out to balance computational efficiency and accuracy, considering the geometry of the corroded surface. Mesh sizes ranging from 0.8 mm to 30 mm, with one to four mesh layers, were evaluated to determine their influence on mechanical properties. The simulation results, shown in Fig. 19, reveal that mesh size significantly affects the stress-strain or load-displacement curves. For this study, mesh sizes of 1 mm for tensile coupons and 5 mm for steel columns were chosen, and the mesh layer for both short and long columns was set at four layers, as illustrated in Fig. 20.

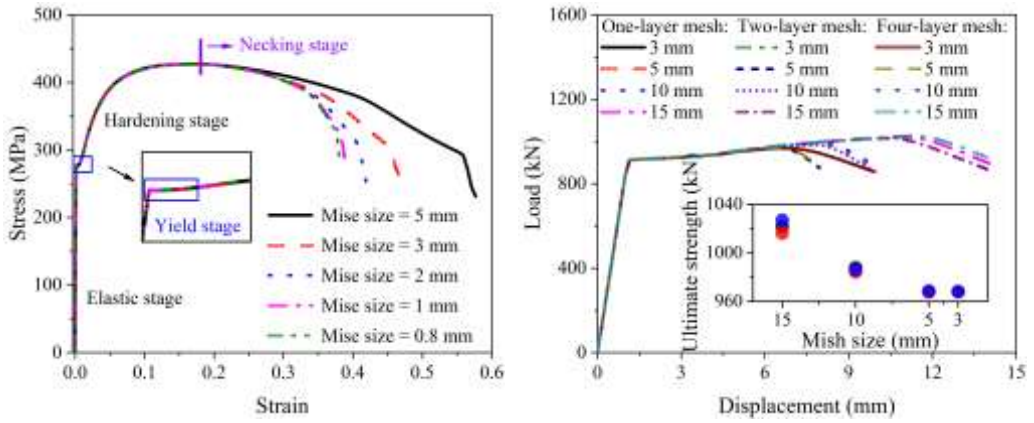

(a) Stress-stain curves of tensile coupons (b) Load-displacement curve of short columns

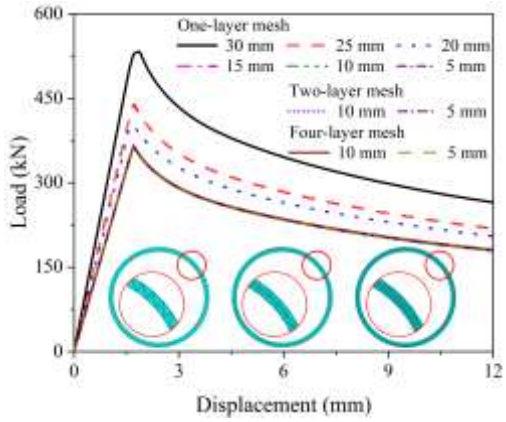

(c) Load-displacement curve of long columns

Fig. 19. Sensitivity analysis of the mesh size.

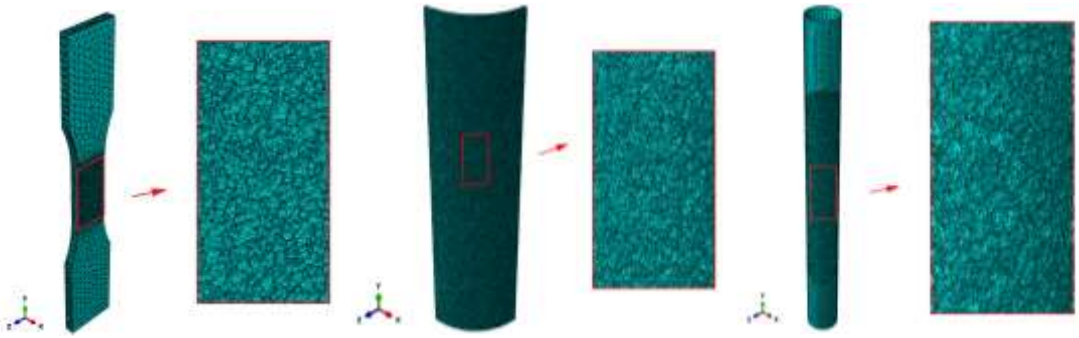

(a) Tensile coupon specimen (b) Short column (c) Long column

Fig. 20. Numerical models with mesh sizes.

5 Verification

The mechanical properties, compression behaviour, and failure modes of the tensile coupon and steel columns with corrosion times of 30 – 270 days were verified against available experimental results. To account for the effects of randomly distributed pit positions, five repeated simulations for each specimen were conducted, mitigating the impact of pit distribution on the mechanical behaviour [24].

5.1 Tensile coupon specimen

Fig. 21 illustrates the distribution of true strain at various stages of evolution, where the true fracture strain was calibrated at 1.31, as discussed in Section 4.1. In this study, sections exhibiting a true strain exceeding 1.31 were identified as fracture cross sections. Notably, the true strain exceeded 1.31 in certain local areas with pit defects, reaching the maximum true strain before

specimen failure. The fracture cross section is clearly discernible when corrosion time is below 150 days. However, at 440 days of corrosion, areas with deep pits and pit groups reach the fracture strain earlier, resulting in specimen fracture.

The stress-strain curves from the test and five simulations are presented in Fig. 22. The simulations align well with the test results across various stages, including elastic, yield plateau, strain hardening, and necking. A ratio (k) of the mechanical property index from the simulation to that of the test was defined. Consequently, values for elastic modulus (E), yield strength (f_y), ultimate strength (f_u), fracture strength (f_f), ultimate strain (ε_u), fracture strain (ε_f), and yield plateau ($\Delta\varepsilon_y$) were derived, as detailed in Table 6. The k values for all indices are between 0.964 and 1.023 at 70 days of corrosion. At 150 days, except for the ultimate strength, k values for the remaining indices range between 0.977 and 1.046. However, at 440 days of corrosion, the elastic modulus in simulations is stable, with a maximum error of 12.12%. The k value for fracture strain varies from 0.95 to 1.132, likely due to localised yield regions caused by pit-induced stress concentration. Thus, the fracture stage is influenced by the characteristics of individual pits and their random distribution, as shown in Fig. 21. Both the pit depth and location have a more significant impact on strain than on stress during corrosion.

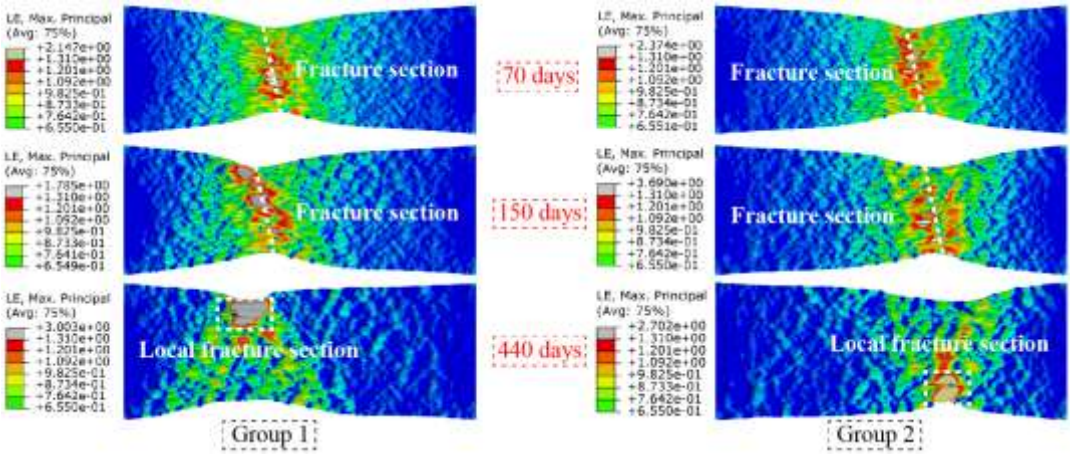

Fig. 21. Fracture mode of the gauge length segment at different corrosion times.

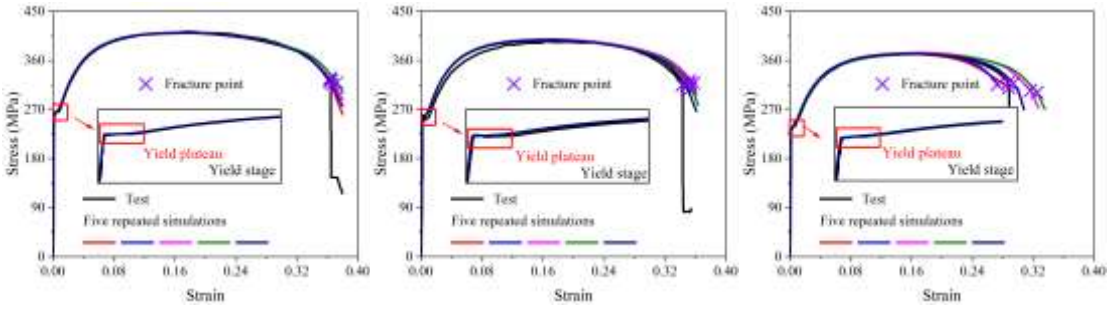

(a) 70 days (B) 150 days (C) 440 days

Fig. 22. Stress-strain curves at different corrosion times.

Table 6 Summary of mechanical property indexes of the numerical model

Corrosion time t (day)	Group	k of E	k of f_y	k of f_u	k of f_f	k of ε_u	k of ε_f	k of $\Delta\varepsilon_y$
70	1	99.36	98.65	99.46	99.11	99.84	99.69	98.19
	2	99.4	98.53	99.51	99	99.81	99.68	97.57
	3	99.39	98.62	99.41	99.02	100.99	100.25	96.37
	4	99.31	98.62	99.36	98.03	100.88	102.29	96.46
	5	99.28	98.54	99.28	97.09	99.33	100.45	101.92
	Mean	99.348	98.592	99.404	98.45	100.17	100.472	98.102
	CoV	0.000	0.000	0.001	0.008	0.007	0.010	0.021
150	1	99.62	99.84	101.1	97.7	92.25	103.55	100.1
	2	102.15	99.69	101.21	101.89	92.13	102.87	99.83
	3	99.72	99.9	101.11	100.8	96.23	104.58	97.55
	4	99.53	99.68	100.83	100.38	94.27	102.94	99.46
	5	99.59	99.76	100.93	98.84	93.84	101.86	98.21
	Mean	100.122	99.774	101.036	99.922	93.744	103.16	99.03
	CoV	0.010	0.001	0.001	0.015	0.016	0.009	0.010
440	1	88.99	96.5	99.36	97.09	95.65	100.28	96.58
	2	89.11	97.11	99.77	99.12	97.16	95	98.32
	3	87.88	97.08	99.91	95.57	104.39	110.11	93.53
	4	88.68	97.08	99.28	94.36	105.55	113.21	97.34

5	89.11	97.43	99.41	99.64	97.07	102.24	96.12
Mean	88.754	97.04	99.546	97.156	99.964	104.168	96.378
CoV	0.005	0.003	0.002	0.021	0.041	0.064	0.017

5.2 Steel CHS short column

The von Mises stress distributions at the failure stage of CHS steel columns are displayed in Fig. 23. The typical failure modes of the FE models, based on the corrosion evolution method, closely match those observed in the tests. The failure mode in the FE model, consistent with the corrosion evolution model, is uniform and occurs at the same location, specifically local buckling in the middle of the columns. Upon failure of the CHS steel columns, the von Mises stress in the local buckling area exceeds the yield stress, while it remains below the yield stress in other areas.

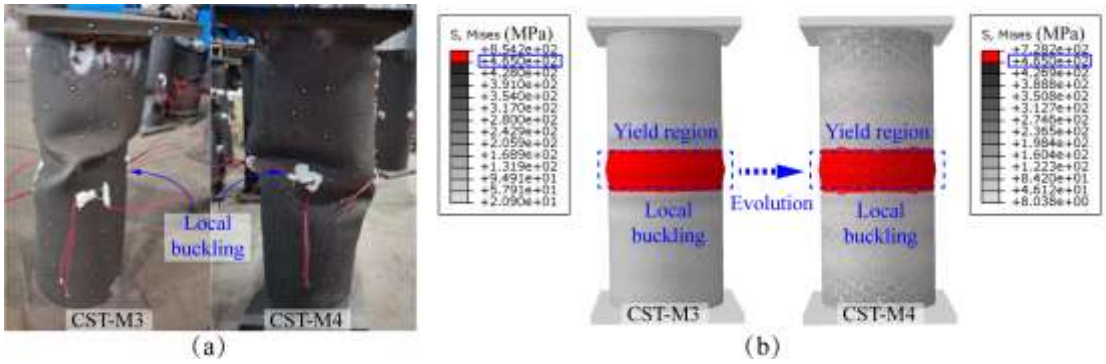

Fig. 23. Failure mode. (a) Test [6], (b) Numerical model.

Fig. 24 displays the load-displacement curves of the steel CHS short column from both simulation and test results. The overall trend of the numerical curve aligns well with that of the test. However, the simulation shows a slightly higher initial stiffness compared to the test, likely due to test setup factors like uneven force application at the loading end, gaps between the column and endplates, and deformation of loading devices, which are not accounted for in the simulation [8 – 9]. Table 7 presents the yield and ultimate loads from five simulations and their averages at each time. The yield strength ratio (k) and ultimate strength ratio (k_u) ranged from 1.011 to 1.037 and 0.934 to 1.027, respectively, with the maximum error between the numerical model and test being 6.57%. The average values of k_y and k_u were 1.019 and 0.982, respectively, underscoring the reliability and accuracy of the developed column models. It is noteworthy that the variability in

yield and ultimate strengths from the numerical results increased with corrosion time, likely due to severely deteriorated surfaces of the corroded members, leading to local failures like premature local buckling.

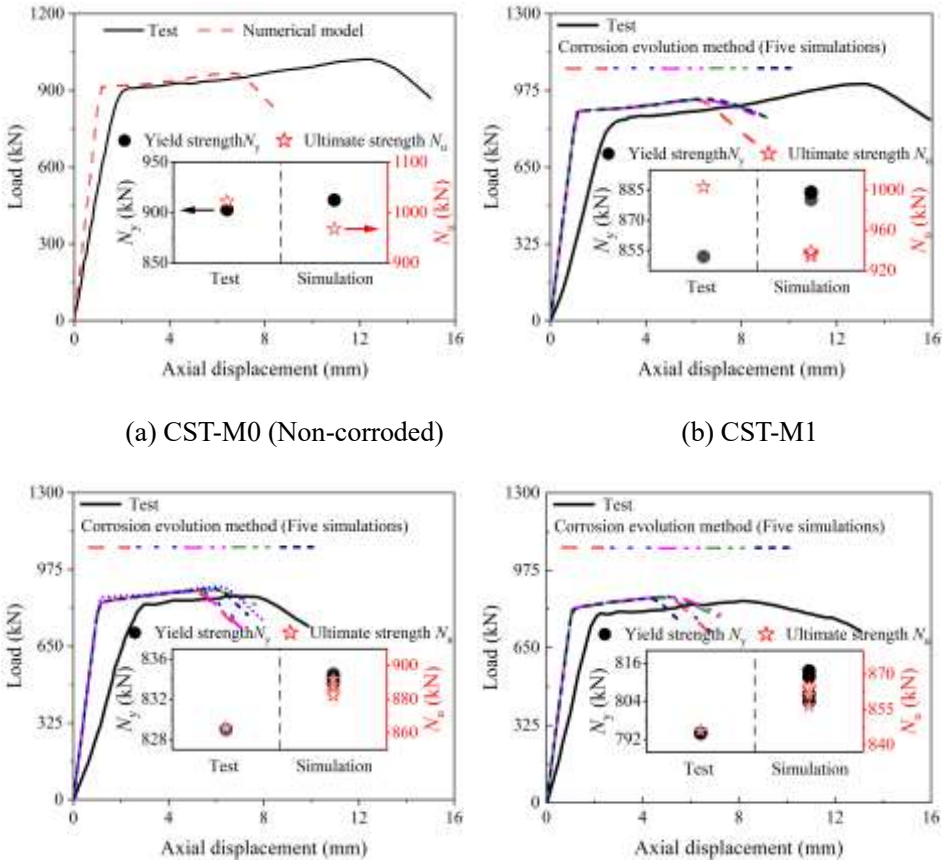

Fig. 24. Load-displacement curves.

Table 7 Summary of yield and ultimate loads

Specimen	Yield load N_y (kN)			Ultimate load N_u (kN)		
	Test [6]	Simulation (average)	k_y	Test [6]	Simulation (average)	k_u
CST-M0	903	912.544	1.011	1022	968.070	0.947
CST-M1	852	883.095	1.037	1003	937.065	0.934
CST-M3	829	833.732	1.006	863	886.060	1.027
CST-M4	794	809.500	1.020	846	862.068	1.019

	Mean	1.019	0.982
	CoV	0.012	0.042

Note: k_y and k_u are ratios of yield and ultimate strengths obtained by simulations to those of tests, respectively.

5.3 Steel CHS long column

The failure modes of the long columns in both test and numerical models are illustrated in Fig. 25. The fracture mode in the FE model corresponds with that observed in the test, namely, global buckling at the midspan of the CHS long column.

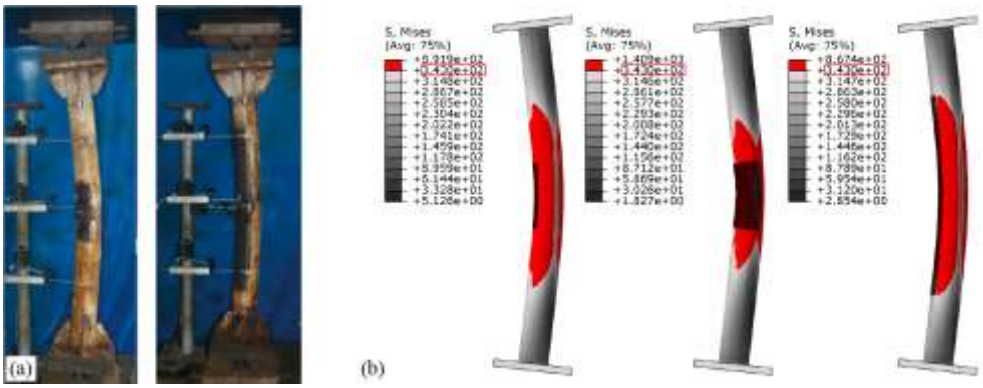

Fig. 25. Failure mode. (a) Test [8], (b) Numerical model.

Fig. 26 shows the load-displacement curves of the long column from both test and simulation, with ultimate strength (N_u) and initial stiffness (S_t) values provided in Table 8. The simulated curves generally mirror the test trends, indicating satisfactory accuracy and reliability of the developed models. The average ultimate strength ratio (k_u) was 1.001 with a coefficient of variation (CoV) of 0.049. However, moderate discrepancies in initial stiffness were noted in specimens H3L1-180 and H1L2-270, similar to the short column cases. The load-displacement curves of the five simulations were almost identical, suggesting minimal impact of random pit distribution on the column's compression behaviour, applicable across slight, moderate, and severe corrosion stages. Nonetheless, scenarios involving local pitting corrosion with significant depth and width fall outside this study's scope; the effects on compressive behaviour of steel CHS long columns in such cases warrant further investigation using the FE model based on the corrosion evolution model.

In summary, the proposed corrosion evolution model effectively assesses the mechanical behaviour of corroded structural members.

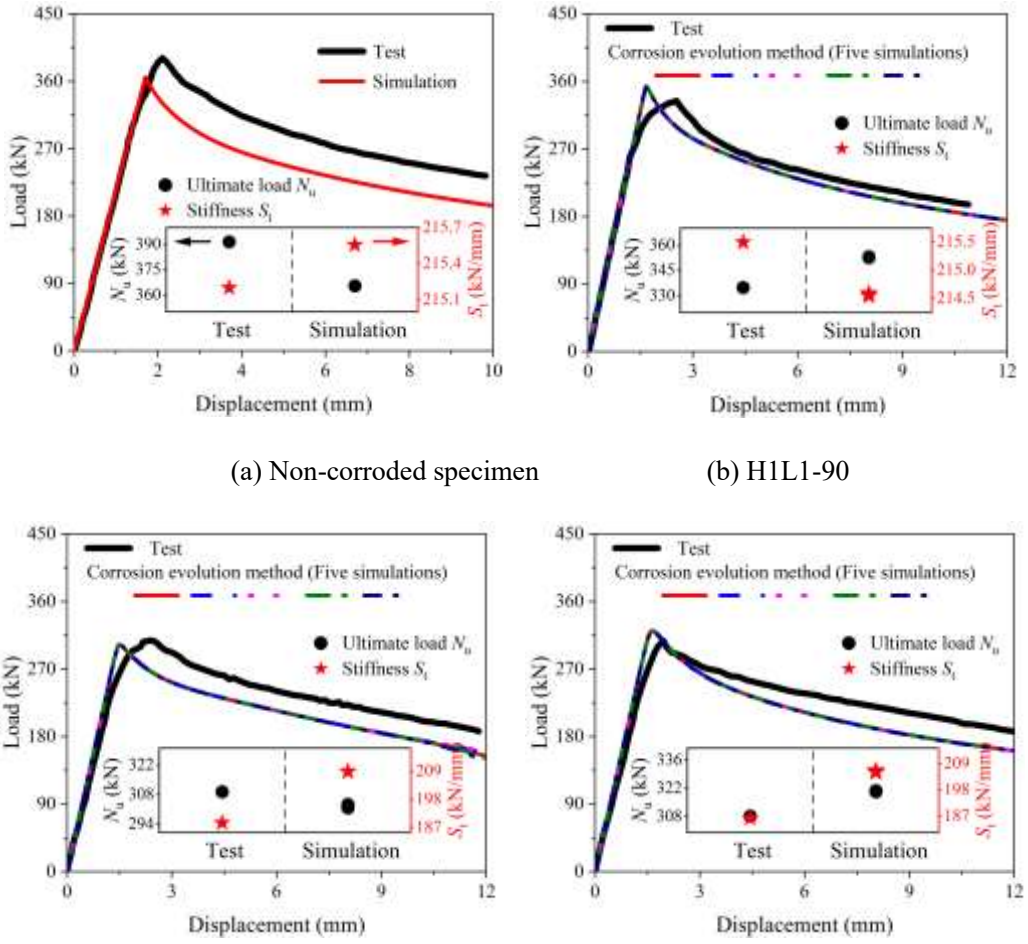

(a) Non-corroded specimen (b) H1L1-90

(c) H3L1-180 (d) H1L2-270

Fig. 26. Load-displacement curves.

Table 8 Summary of ultimate load and stiffness

Specimen	Ultimate load N_u (kN)			Stiffness S_t (kN/mm)		
	Test [8]	Simulation (average)	k_u	Test [8]	Simulation (average)	k_s
Non-corroded	391.5	365.421	0.933	215.2	215.557	1.002
H1L1-90	334.8	352.863	1.054	215.5	214.569	0.996
H3L1-180	309.3	302.535	0.978	188.8	208.889	1.106
H1L2-270	308.2	320.613	1.040	186.2	205.917	1.106
		Mean	1.001			1.053
		CoV	0.049			0.051

Note: k_u and k_s are ratios of ultimate load and stiffness obtained by simulations to those of tests,

512 respectively.

513 6 Discussions

514 The thickness reduction approach is commonly employed in engineering to predict the
515 mechanical behaviour of corroded members post corrosion [8, 24]. Thus, a comparison between the
516 proposed corrosion evolution and the thickness reduction method was undertaken.

517 Fig. 27 compares the yield strengths of steel CHS short columns obtained from the test [6] and
518 FE models based on both the proposed corrosion evolution and thickness reduction methods. The
519 simulation results of the FE models, developed using the proposed corrosion evolution method and
520 the thickness reduction method, are detailed in Tables 7 and 9, respectively. Similarly, Fig. 27(b)
521 presents the ultimate strengths of steel CHS long columns experiencing global buckling, as
522 calculated using both methods, with corresponding simulation results in Tables 8 and 9. The
523 relationship between yield strength and corrosion time was modelled using a power function, as
524 expressed in Eq. (10), with calibrated parameters listed in Table 10. Ratios of yield strengths derived
525 from FE models based on the thickness reduction (k_t) and corrosion evolution methods (k_p) to the
526 test results are shown in Fig. 27. The comparison reveals that yield strengths obtained from
527 simulations using the thickness reduction method were generally higher than the test results, with
528 the ratio k_t increasing over time. However, yield strengths from FE models based on the corrosion
529 evolution method closely matched the test results, maintaining a relatively stable k_p ratio throughout
530 the calculated corrosion period. This improved accuracy is attributed to the corrosion evolution
531 method's ability to account for local defects induced by pits.

532 Based on this foundation, it is important to note that not only did the corrosion patterns
533 observed in the fabricated CHS steel columns closely resemble the actual measurements, but the
534 mechanical performance predicted by the FE models, utilising the proposed corrosion evolution
535 approach, proved to be more precise and reliable when compared to models based on the thickness
536 reduction method. Therefore, the proposed corrosion evolution method is recommended for
537 predicting the residual mechanical behaviour of CHS columns in corrosive environments.

538 $$N_y(N_u) = F + Gt^n \tag{10}$$

539 where N_y and N_u are the yield and ultimate strengths, and F, G, and n are the parameters controlling
540 the curve shape.

Table 9 Simulation results of the thickness reduction method

CHS short column		CHS long column	
Model	Yield strength/MPa	Model	Ultimate strength/MPa
CST-M0	912.544	Non-corroded	365.421
CST-M1	888.918	H1L1-90	357.112
CST-M3	857.272	H3L1-180	320.989
CST-M4	843.737	H1L2-270	337.454

Table 10 Parameters of F and G

Specimen	Method	F	G
Short column	Test [6]	893.927	-2.498
	Thickness reduction	912.544	-1.867
	Corrosion evolution	912.544	-2.654
Long column	Test [8]	371.617	-0.935
	Thickness reduction	365.195	-0.476
	Corrosion evolution	368.198	-0.746

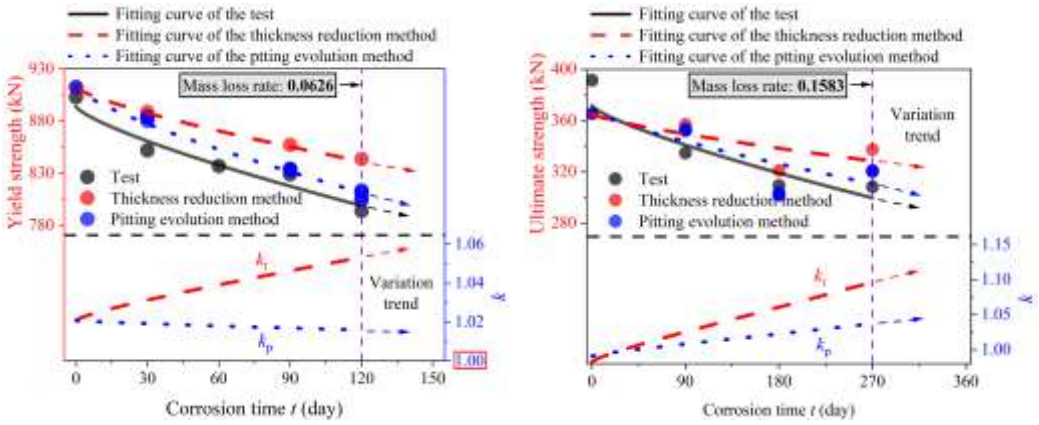

(a) Circular steel short column (b) Circular steel long column

Fig. 27. Comparison of thickness reduction with corrosion evolution methods.

7 Conclusions

This study introduced a corrosion evolution model by characterising the corrosion morphology

and calibrating parameters throughout the entire corrosion period. The model enabled the numerical reproduction of the corrosion evolution process. FE models of corroded steel tensile coupons and CHS columns at various stages of corrosion were developed and validated against experimental results. Additionally, FE models based on the conventional uniform thickness reduction method for corroded specimens were also established for comparative analysis. The key findings are summarised as follows:

(1) The thickness loss, pit depth, and pit aspect ratio were identified as crucial parameters in the proposed corrosion evolution model. This model was based on the premise that the number of pits in the corrosion morphology remained constant, and the time-varying pit aspect ratio stayed consistent. An interpolation approach was used to determine the number of pits from the measured thickness loss during corrosion. Consequently, corrosion morphologies were generated using the proposed model and calculated pit number, based solely on the known corrosion ratio.

(2) The novel corrosion evolution method was successfully integrated into FE models and validated at both material and member levels, specifically for tensile coupons and columns. The developed FE models for corroded steel coupons and members accurately replicated structural behaviour, including stress-strain curves, load-displacement curves, and failure modes, at specific corrosion times.

(3) The proposed corrosion evolution method, combined with an interpolation approach, allowed for the accurate reproduction of corrosion morphologies with randomly distributed corrosion pits. Only the experimentally measured corrosion ratio was required to determine pit number and random pit morphology. Therefore, FE models incorporating corrosion evolution morphologies could be developed using this method with standard experimental data, such as corrosion ratio.

(4) A comparison between FE models based on the proposed corrosion evolution and conventional uniform thickness reduction methods was conducted to evaluate the effectiveness of the proposed numerical simulation method in predicting the structural behaviour of corroded steel members. The models employing the corrosion evolution approach demonstrated superior performance in predicting the mechanical behaviour of corroded members, particularly in instances of severe corrosion damage.

Declaration of Competing Interest

The authors declare that they have no known competing financial interests or personal relationships that could have appeared to influence the work reported in this paper.

Acknowledgements

The authors would like to sincerely acknowledge the support from the National Natural Science Foundation of China (52378130 and 52221002) and the Natural Science Foundation of Chongqing (CSTB2023NSCQ-MSX0576).

References

[1] O. Adedipe, F. Brennan, A. Kolios, Review of corrosion fatigue in offshore structures: present status and challenges in the offshore wind sector, Renew. Sustain. Energy Rev., 61 (2016), 141-154, https://doi.org/10.1016/j.rser.2016.02.017.

[2] R.E. Melchers, Recent progress in the modelling of corrosion of structural steel immersed in seawaters, J. Infrastruct. Syst. 12 (2006) 154-162, https://doi.org/10.1061/(ASCE)1076-0342(2006)12:3(154).

[3] B. Nie, S. Xu, J. Yu, H. Zhang, Experimental investigation of mechanical properties of corroded cold-formed steels, J. Constr. Steel Res., 162 (2019), 105706, https://doi.org/10.1016/j.jcsr.2019.105706.

[4] M.Y. Yang, S. Kainuma, W. Nabeshima, W. Yamauchi, B. H. Ji, Synergistic effect of corrosion and residual stress on fatigue cracks of finger-type bridge expansion joints, Eng. Fail. Anal., 131 (2022), 105894, https://doi.org/10.1016/j.engfailanal.2021.105894.

[5] C. Jia, Y. Shao, L. Guo, Y. Liu, Mechanical properties of corroded high strength low alloy steel plate, J Constr Steel Res, 172 (2020), 106160, https://doi.org/10.1016/j.jcsr.2020.106160.

[6] S.S. Song, X. Liu, J. Chen, C.H. Ye, J. Liu, C.B. Liu. Compressive behaviour of corroded thin-walled circular section steel stub columns, Thin-Walled Struct., 180 (2022), 109794, https://doi.org/10.1016/j.tws.2022.109794.

[7] H.J. Wang, Z.W. Zhang, H.L. Qian, F. Fan. Effect of local corrosion on the axial compression behaviour of circular steel tubes. Eng Struct, 224 (2022), 111205, https://doi.org/10.1016/j.engstruct.2020.111205.

[8] Y. Wei, Z.Q. Wu, X.T. Wang, S.F. Jiang, Mechanical behavior of locally corroded circular steel tube under compression, Structures, 33 (2021), 776-791, https://doi.org/10.1016/j.istruc.2021.04.063.

[9] S. Gao, Y.L. Wang, L.H. Guo, Y.C. Xu, J. Iyama. Axial behavior of circular steel tube with

localized penetrating corrosion simulated by artificial notch, Thin-Walled Struct., 172 (2022), 108944, https://doi.org/10.1016/j.tws.2022.108944.

[10] J.H. Ahn, W.R. Choi, S.H. Jeon, S.H. Kim, I.T. Kim. Residual compressive strength of inclined steel tubular members with local corrosion. Appl. Ocean. Res., 59 (2016) 498-509, http://dx.doi.org/10.1016/j.apor.2016.07.002.

[11] A. Valor, F. Caleyo, L. Alfonso, D. Rivas, J.M. Hallen. Stochastic modeling of pitting corrosion: A new model for initiation and growth of multiple corrosion pits, Corros. Sci., 49 (2007) 559–579, https://doi.org/10.1016/j.corsci.2006.05.049.

[12] A. Valor, F. Caleyo, D. Rivas, J.M. Hallen. Stochastic approach to pitting-corrosion-extreme modelling in low-carbon steel, Corros. Sci., 52 (2010) 910–915, https://doi.org/10.1016/j.corsci.2009.11.011.

[13] Z. Meng, F.L. Wang, G.X. Shi. A novel evolution model of pitting failure and effect on time - varying meshing stiffness of spur gears. Eng. Fail. Anal., 2021;120:105068. https://doi.org/10.1016/j.engfailanal.2020.105068.

[14] G.J. Qin, Y. F. Cheng, P. Zhang, Finite element modeling of corrosion defect growth and failure pressure prediction of pipelines, Int. J. Pres. Ves. Pip., 194 (2021) 104509, https://doi.org/10.1016/j.ijpvp.2021.104509.

[15] H.K. Wang, Y. Yu, J.X. Yu, W.P. Xu, H.C. Chen, Z.Y. Wang, M.X. Han, Effect of pitting defects on the buckling strength of thick-wall cylinder under axial compression, Constr. Build. Mater., 224 (2019) 226-241, https://doi.org/10.1016/j.conbuildmat.2019.07.074.

[16] Z.W. Zhang, H.J. Wang, H.L. Qian, F. Fan. Parameter sensitivity analysis and evaluation method of axial compression bearing capacity of corroded circular steel tubes, Thin-Walled Struct., 163 (2021) 107699, https://doi.org/10.1016/j.tws.2021.107699.

[17] H.K. Wang, Y. Yu, J.X. Yu, C.H. Jin, Y. Zhao, Z.Y. Fan, Y. Zhang, Effect of 3D random pitting defects on the collapse pressure of pipe - Part II: Numerical analysis, Thin-Walled Struct., 129 (2018) 527-541, https://doi.org/10.1016/j.tws.2018.04.014.

[18] H. Wu, H.S. Zhao, X. Li, X. Feng. Elastic-plastic buckling of pipes with asymmetric dual corrosion defects subject to external pressure, Ocean Eng., 240 (2021) 109975, https://doi.org/10.1016/j.oceaneng.2021.109975.

[19] A. A. Soliman, M. M. Megahed, Ch.A.R. Saleh, M. Shazly, Pressure carrying capacities of thin walled pipes suffering from random colonies of pitting corrosion, Int. J. Pres. Ves. Pip., 2018,166 (2018) 48-60, https://doi.org/10.1016/j.ijpvp.2018.08.003.

[20] R.H. Wang, H.C. Guo, R.A. Shenoi, Experimental and numerical study of localized pitting effect on compressive behavior of tubular members, Mar. Struct. 72 (2020) 102784, https://doi.org/10.1016/j.marstruc.2020.102784.

[21] X.W. Zhang, S.L. Zhao, Z. Wang, J.X. Li, L.J. Qiao, The pitting to uniform corrosion evolution process promoted by large inclusions in mooring chain steels, Mater. Charact., 181 (2021) 111456, https://doi.org/10.1016/j.matchar.2021.111456.

[22] C.Q. Cheng, L.I. Klinkenberg, Y. Ise, J. Zhao, E. Tada, A. Nishikata, Pitting corrosion of sensitised type 304 stainless steel under wet-dry cycling condition, Corros. Sci., 118 (2017) 217-226, https://doi.org/10.1016/j.corsci.2017.02.010.

[23] A. Racot, I. Aubert, M. Touzet, S. Thiebaut, M. Demesy, Statistical analysis of the pitting corrosion induced by potentiostatic pulse tests of wrought and SLM 316L stainless steels, Corros. Sci., 197 (2022) 110036, https://doi.org/10.1016/j.corsci.2021.110036.

[24] Y. Zhao, Q. Guo, Z.Z. Zhao X. Wu, Y. Xing. Prediction of tensile strength degradation of corroded steel based on in-situ pitting evolution, Steel Compos. Struct., 46 (2023), 385-401, https://doi.org/10.12989/scs.2023.46.3.385.

[25] D. Rivas, F. Caleyo, A. Valor, J.M. Hallen, Extreme value analysis applied to pitting corrosion experiments in low carbon steel: Comparison of block maxima and peak over threshold approaches. Corros. Sci., 50(2008) 3193-3204, https://doi.org/10.1016/j.corsci.2008.08.002.

[26] M. Xia, Y.D. Wang, S.H. Xu, Study on surface characteristics and stochastic model of corroded steel in neutral salt spray environment, Constr. Build. Mater., 2021,272 (2021) 121915, https://doi.org/10.1016/j.conbuildmat.2020.121915.

[27] Y.Q. Zhou, D. L. Engelberg, Time-lapse observation of pitting corrosion in ferritic stainless steel under bipolar electrochemistry control, J. Electroanal. Chem., 899 (2021) 115599, https://doi.org/10.1016/j.jelechem.2021.115599.

[28] C.J. Cui, R.J. Ma, A.R. Chen, Z.C. Pan, H. Tian, Experimental study and 3D cellular automata simulation of corrosion pits on Q345 steel surface under salt-spray environment, Corros. Sci., 154(2019) 80-89, https://doi.org/10.1016/j.corsci.2019.03.011.

[29] P. J. Denissen, S. J. Garcia, Reducing subjectivity in EIS interpretation of corrosion and corrosion inhibition processes by in-situ optical analysis, Electrochim. Acta, 293 (2019) 514-524, https://doi.org/10.1016/j.electacta.2018.10.018.

[30] Q. Guo, Y. Zhao, Y. Xing, J.F. Jiao, B.Z. Fu, Y.Q. Wang. Experimental and numerical analysis of mechanical behaviors of long-term atmospheric corroded Q235 steel, Structures, 39 (2022) 115-131, https://doi.org/10.1016/j.istruc.2022.03.027.

[31] S. Shojai, P. Schaumann, T. Brömer, Probabilistic modelling of pitting corrosion and its impact on stress concentrations in steel structures in the offshore wind energy, Mar. Struct., 84 (2022) 103232, https://doi.org/10.1016/j.marstruc.2022.103232.

[32] H.Y. Wu, H.G. Lei, C. Y. Frank, Study on corrosion models of structural steel exposed in urban industrial atmospheric and laboratory simulated environments based on the 3D profile, Thin Walled Struct., 168 (2021) 108286, https://doi.org/10.1016/j.tws.2021.108286.

[33] S.H. Xu, C.M. Song, H. Li, Difference in surface characteristics of corroded steel under simulated marine and general atmosphere environment, Mater. Rep., 35 (2021) 2125-2132, https://doi.org/10. 11896 /cldb. 19110139, (in Chinese)

[34] Y.D. Wang, T. Shi, H.J. Zhang, B. Nie, H. Wang, S.H. Xu. Hysteretic behavior and cyclic constitutive model of corroded structural steel under general atmospheric environment, Constr.

692 Build. Mater., 2021,270,121474, https://doi.org/10.1016/j.conbuildmat.2020.121474.

693 [35] N. Gathimba, Y. Kitane, Effect of surface roughness on tensile ductility of artificially corroded
694 steel plates, J. Constr. Steel Res., 2021,176 (2021) 106392,
695 https://doi.org/10.1016/j.jcsr.2020.106392.

696 [36] C. Jia, Y.S. Shao, L.H. Guo, H.J. Huang. Surface topography and stress concentration analysis
697 for corroded high strength steel plate, J. Constr. Steel Res., 187 (2021) 106952,
698 https://doi.org/10.1016/j.jcsr.2021.106952.

699 [37] H. Wang, S.H. Xu, Study on mechanical properties degradation laws of corroded welded steel
700 plates under monotonic and cyclic loading. China Civ. Eng. J., 55 (2022):10-25,
701 https://doi.org/10.15951/j.tmgcxb.21101029. (in Chinese)

702 [38] J. Daidola, J. Parente, I. Orisamolu, K. Ma,. Residual Strength Assessment of Pitted Plate
703 Panels. Ship Structure Committee, Washington DC, 1997, 17–91. USA.

704 [39] Y.L. He. Experimental study on monotonic tensile behavior of corroded steel in neutral salt
705 spray environment. Xi'an University of Architecture and Technology, 2015.

706 [40] Y. Ling. Uniaxial True Stress-Strain after Necking. AMP Journal of Technology, 2004.

707 [41] L.J. Jia, H. Kuwamura, Ductile fracture simulation of structural steels under monotonic tension,
708 J. Struct. Eng.-ASCE, 140 (2014), https://doi.org/10.1061/(ASCE)ST.1943-541X.0000944.

709 [42] K. Woloszyk, Y. Garbatov, Random field modelling of mechanical behaviour of corroded thin
710 steel plate specimens, Eng. Struct., 212 (2020) 110544,
711 https://doi.org/10.1016/j.engstruct.2020.110544.

712 [43] X. Yun, L. Gardner, Stress-strain curves for hot-rolled steels, J. Constr. Steel Res., 133(2017)
713 36-46, https://doi.org/10.1016/j.jcsr.2017.01.024.

714 [44] Y. Wei, Z.Q. Wu, X.T. Wang, S.F. Jiang. Degradation law and time-varying model of
715 mechanical properties of corroded Q235 steel in offshore atmospheric environment. J. Water
716 Resour. Archit. Eng., 19 (2021) 60-66, https://doi.org/10.3969/j.issn.1672-1144.2021.04.010.
717 (in Chinese)

718 [45] B. Y. Zhao. The research on the method of testing the cold-formed thin-walled steel's remnant
719 stress and the member's whole stability of axially loaded compression with remnant stress.
720 Wuhan University of Science and Technolog, 2006. (in Chinese)

721 [46] F. Xu, T.M. Chan, T. Sheehan, L. Gardner. Prediction of ductile fracture for circular hollow
722 section bracing members under extremely low cycle fatigue, Eng. Struct. 214 (2020) 110579,
723 https://doi.org/10.1016/j.engstruct.2020.110579.

724